

## Supplementary material: Methodology and full results

Zoltán Sylvester, Paul Durkin, Jacob A. Covault

The channel centerline data was derived from georeferenced Landsat images, downloaded from the Earth-Explorer USGS website (<https://earthexplorer.usgs.gov/>). True-color images were created to quality check and refine the mapping results in the QGIS package (<https://qgis.org/>). To increase the speed of interpretation and improve reproducibility, we have detected channel centerlines using a quasi-automated workflow, based on the Python package RivaMap, developed by Isikdogan et al. (2015, 2017). The input to the RivaMap algorithm is the Modified Normalized Difference Water Index (MNDWI; Xu, 2006). In the MNDWI image, rivers are identified using the multiscale singularity index, an index that enhances curvilinear features. Once the curvilinear bodies of water are highlighted, river centerlines are generated through non-maxima suppression along the dominant orientation. For additional details on the RivaMap centerline generation see Isikdogan et al. (2017). We have used Jupyter notebooks (Kluyver et al. 2016; <http://jupyter.org/>) to perform the data analysis and modeling.

The RivaMap package can be used to generate centerlines for the larger channels in the Landsat scene but it does not create a single continuous centerline for the channel of interest. Therefore, we have written a new workflow to extract the centerline of the river as an upstream-to-downstream ordered array of pixel locations. This workflow is not entirely automated, as the centerline needs to be manually edited using image editing software, but it is still less time consuming and more reproducible than an entirely manual interpretation. To obtain relatively smooth centerlines from the pixel-based data points, we have applied a Savitzky-Golay filter (Savitzky and Golay, 1964), with a footprint of 21 points; then, to reduce the noise in the curvature data, we have resampled and smoothed the centerlines and the banks again, by using a B-spline representation (Figure 1). Each centerline was resampled to a 25 m spacing between consecutive points. Curvature was computed at every point using Cartesian coordinates:

$$C = \frac{x'y'' - y'x''}{(x'^2 + y'^2)^{3/2}}, \quad (1)$$

where  $x'$  and  $x''$  are first and second-order derivatives of  $x$ . Derivatives were computed using second order accurate central differences in the numpy Python package.

Once the channels are extracted from each Landsat scene, migration rates can be estimated using two consecutive pairs of channel centerlines. We have chosen the time gap between images so that there is enough change in low-curvature bends to get a good signal, yet the change in high-curvature bends does not render the migration measurement meaningless. For the slower-migrating rivers, this means a time gap of about 30 years. To speed up the computation of migration rate, we do this by using a dynamic time warping algorithm (DTW), an algorithm that is often used to correlate two time series and relies on dynamic programming (Lisiecki and Lisiecki, 2002; Figure 2B). The distance (or cost) matrix consists of the Euclidian distances between each pair of centerline points; and the correlation consists of finding a path from one corner of this matrix to the diametrically opposed corner and to minimize the sum of the distances along the path. To speed up calculations, we have used the `dp_python` module ([https://github.com/dpwe/dp\\_python](https://github.com/dpwe/dp_python)), which relies on a C routine for the computationally most expensive part of the algorithm. Although this approach is comparable to a simple nearest neighbor search, the results are different: using DTW avoids large gaps between correlated points on the second centerline (Figure 2). Figure 2 also illustrates the difference between 'bank migration' and 'bend migration'; the primary mechanism that we are interested in and the one that is directly related to shear stress along the banks is bank migration. The difference between the two is significant in the case of downstream translating bends, and is analogous to the difference between wave speed and particle velocity.

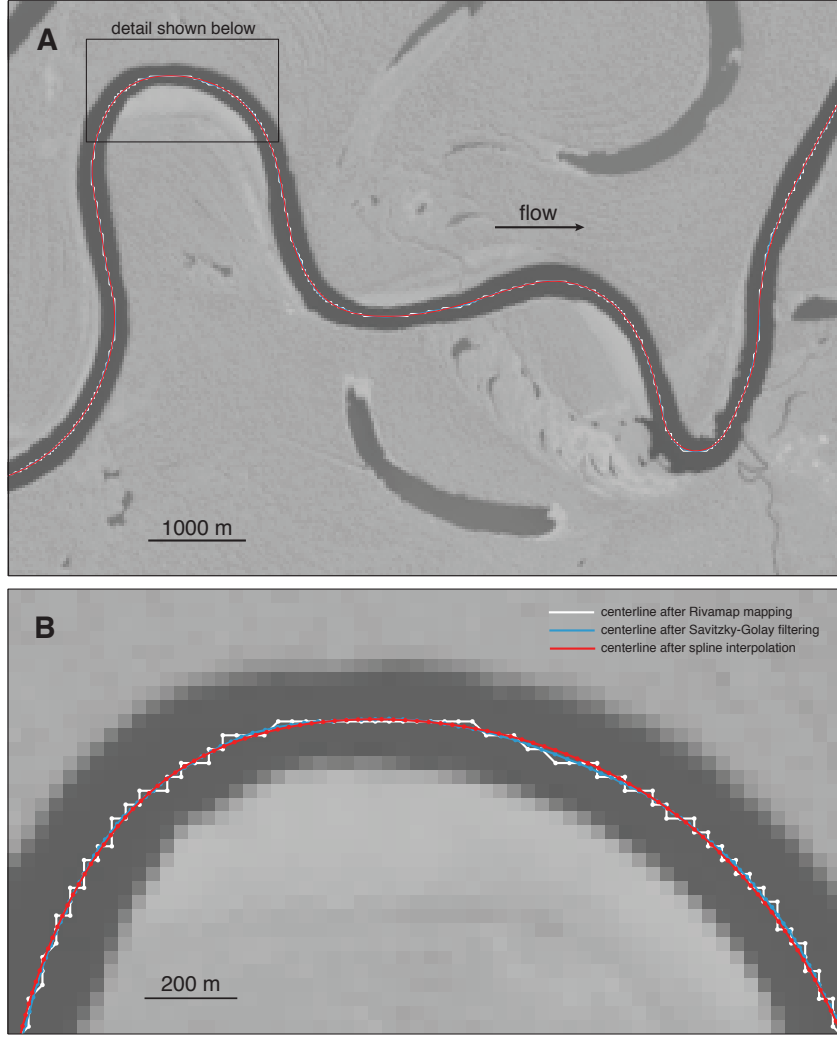


Figure 1: Example of centerline mapping results. (A) Centerline extraction results plotted over a modified normalized water index image of the Juruá River. (B) Zoomed-in detail of (A), showing the result of tracking the skeletonized centerline in the Rivamap output (white), the effect of the Savitzky-Golay filtering (blue), and the final result after spline interpolation (red).

To be consistent with the Howard and Knutson meandering model, the migration rate should be computed along a line perpendicular to the channel centerline, so the question arises how different the DTW technique is from the 'perpendicular' approach. We have found that, if the distances between the centerlines and between the points along the centerlines are not too large, the nearest-point approach gives a good approximation of the migration distances in the perpendicular direction (Figure 2). The advantage of the DTW approach is that the correlated point spacing on the second centerline remains unchanged. In addition, the DTW approach is computationally efficient.

Once computed, both the curvature and the migration rate series have been smoothed using a Savitzky-Golay filter.

Next, the nominal migration rate is estimated:

$$R_0 = k_l W C, \quad (2)$$

where  $k_l$  is the migration rate constant,  $W$  is channel width, and  $C$  is curvature ( $1/R$ ). We do not assume that, above a critical curvature value, the nominal migration rate should decrease with increasing curvature (e.g., Howard and Knutson, 1984). To estimate migration rates that are only dependent on the local and

upstream curvatures, we use the Howard and Knutson (1984) model, which is based on the calculation of an adjusted channel migration rate  $R_1$  from the nominal migration rate  $R_0$ , using an exponential weighting function  $G(\xi)$ :

$$R_1(s) = \Omega R_0(s) + \left( \Gamma \int_0^\infty R_0(s - \xi) G(\xi) d\xi \right) \left( \int_0^\infty G(\xi) d\xi \right)^{-1} \quad (3)$$

The migration rate constant (or erodibility)  $k_l$  is not known, but we can use an initial guess knowing that the actual migration rate is somewhat larger than the nominal migration rate: for an idealized bend with constant curvatures, equation (3) simplifies to

$$R_1 = 1.5R_0. \quad (4)$$

Using this initial guess for  $k_l$ , we can compute the predicted migration rate using equation (3). To do this we also need river depth  $D$ ; we have estimated river widths from the satellite images and used the following regression between width and depth (Konsoer et al., 2013) to obtain  $D$ :

$$W = 18.8D^{1.41}. \quad (5)$$

The friction factor  $C_f$  is the primary driver of how much phase shift there is between the predicted and actual migration rates. We have optimized the value of  $C_f$  so that this phase shift is at a minimum. We have found that estimates for  $C_f$  have a range of 0.003-0.009 (Table 1). These values are similar to the ones previously published for large rivers (Konsoer et al., 2013).

Finally, our initial estimate for  $k_l$  can be improved by minimizing the mismatch between the amplitude of the actual and predicted migration rates; we have used the 75th percentile to do this.

Bends that were likely affected by cutoff events or reduced erodibility associated with the erosional scarps of the incised valleys have been identified and flagged (Fig. 3). Bends that originate from recent cutoff events tend to have high curvatures and short arc lengths and, as a result, they rapidly migrate downstream (e.g., Fig. 3A). Bends that impinge on the erosional boundary of the channel belt typically show low rates of migration (Fig. 3B).

Having computed these parameters, we can visually compare them by plotting curvature and actual migration rates side-by-side (Figs. 4-6) and plotting the nominal, actual, and predicted migration rates using scatterplots (Figs. 7-10). Map-view comparisons of predicted and actual channel locations are also shown in Figs. 11-12.

Code is available at <https://github.com/zsylvester/curvaturepy>.

## REFERENCES CITED

- Howard, A.D., and Knutson, T.R., 1984, Sufficient conditions for river meandering: A simulation approach: Water Resources Research, v. 20, p. 16591667, <https://doi.org/10.1029/WR020i011p01659>.
- Isikdogan, F., Bovik, A., and Passalacqua, P., 2017, RivaMap: An Automated River Analysis and Mapping Engine: Remote Sensing of Environment, v. 202, p. 88-97, doi:10.1016/j.rse.2017.03.044.
- Kluyver, T., Ragan-Kelley, B., Prez, F., Granger, B.E., Bussonier, M., Frederic, J., Kelley, K., 2016, Jupyter Notebooks - a publishing format for reproducible computational workflows. In: Positioning and power in academic publishing players, agents and agendas, edited by F. Loizides and B. Schmidt, p. 87-90, IOP Press.
- Konsoer, K., Zinger, J., and Parker, G., 2013, Bankfull hydraulic geometry of submarine channels created by turbidity currents: Relations between bankfull channel characteristics and formative flow discharge: Journal of Geophysical Research: Earth Surface, v. 118, p. 216-228, doi:10.1029/2012jf002422.

Table 1: Summary of results for all river segments

Segment	No. of points	No. of bends	Width (m)	Lag (m)	Lag/width	Cf	kl (m/yr)	R(C,M)*	R(M',M)†	P90(M)‡
Juruá	19257	149	242.10	1073	4.43	0.0027	20.00	0.729	0.756	9.56
Juruá 2	11663	99	229.61	811	3.53	0.0039	22.00	0.796	0.798	9.15
Juruá T A	9165	126	119.56	441	3.69	0.0060	12.00	0.763	0.752	5.43
Juruá T B	11319	151	149.62	569	3.80	0.0049	11.00	0.781	0.769	4.64
Purus	18700	123	276.21	1072	3.88	0.0029	26.00	0.702	0.699	12.62
Purus 2	15490	96	300.78	1212	4.03	0.0036	22.00	0.838	0.844	9.52
Jutaí A	8541	149	123.27	310	2.51	0.0076	4.00	0.860	0.854	1.75
Jutaí B	8045	73	260.78	552	2.12	0.0068	4.00	0.717	0.692	2.24
Yavarí A	13930	226	137.35	394	2.87	0.0068	2.00	0.751	0.772	1.46
Yavarí B	5366	51	232.78	610	2.62	0.0049	4.00	0.747	0.764	2.24
Yavarí trib.	8668	136	113.04	407	3.60	0.0053	4.00	0.784	0.774	1.79
Tarauacá A	8803	140	94.59	444	4.69	0.0039	31.00	0.646	0.637	12.71
Tarauacá B	3244	33	146.81	534	3.64	0.0047	24.00	0.807	0.7907	10.22
Mamoré A	8971	92	226.16	647	2.86	0.0076	60.00	0.779	0.771	38.97
Mamoré B	7341	61	314.27	912	2.90	0.0045	128.00	0.642	0.625	82.04

\*correlation coefficient between nominal and actual migration rates

†correlation coefficient between predicted and actual migration rates

‡90<sup>th</sup> percentile of migration rate

Lisiecki, L.E., and Lisiecki, P.A., 2002, Application of dynamic programming to the correlation of paleoclimate records: Paleoceanography, v. 17, 1049, <https://doi.org/10.1029/2001PA000733>.

Savitzky, A., and Golay, M.J.E., 1964, Smoothing and differentiation of data by simplified least squares procedures: Analytical Chemistry, v. 36, p. 1627-1639, doi:10.1021/ac60214a047.

Xu, H., 2006. Modification of normalised difference water index (NDWI) to enhance open water features in remotely sensed imagery. International Journal of Remote Sensing, v. 27, p. 30253033.

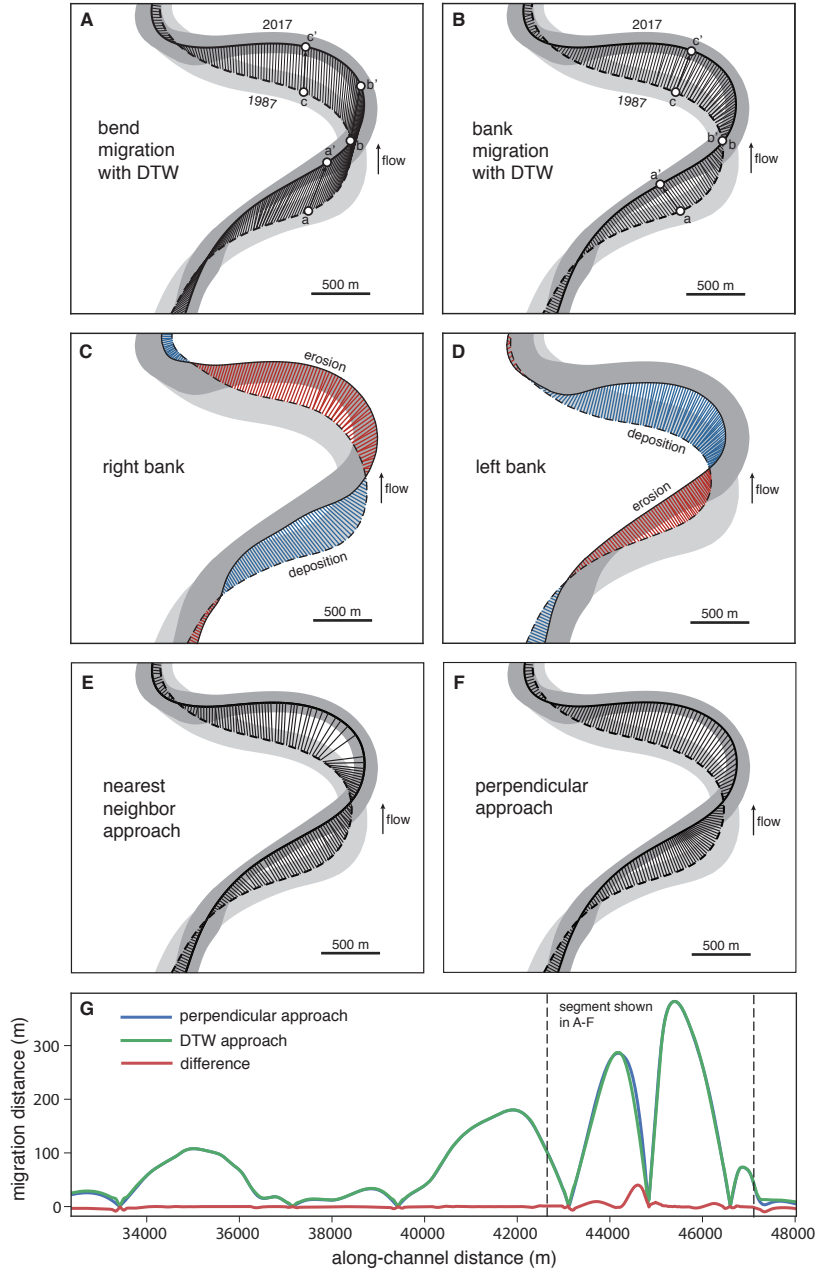


Figure 2: Different ways of measuring local migration rate. We have used the 'bank migration' approach in this study, shown in (B). (A) Migration vectors that correspond to 'bend migration', in a bend that shows significant translation. Every point on the centerline from 1987 is correlated to a point on the centerline from 2017, minimizing the differences in curvature, using dynamic time warping. Inflection points correlate to inflection points. In this interpretation, the point where the two centerlines cross each other (the 'point of no migration') moves about 500 m, from b to b'. (B) If the correlation minimizes the Euclidian distance between centerline points, the resulting migration vectors are averages of how much the banks have moved, and the point of no migration is stationary (b is the same as b'). The result shown here also relies on dynamic time warping. (C) and (D) Changes in the locations of the banks. Migration vectors shown have been computed using the same approach (dynamic time warping that minimizes Euclidian distance) as in (B). Note similarity of bank erosion/deposition patterns with centerline migration in (B). (E) Migration vectors for each point on 1987 centerline, computed using a nearest neighbor search on a k-d tree. Results are quite different from (B), especially for segments with high curvature. (F) Migration vectors that are drawn in a direction perpendicular to the 1987 centerline. Overall similar pattern to dynamic time warping approach shown in (B), but sampling along the more recent centerline is unequal. (G) Comparison between migration distances calculated using the 'perpendicular' approach (F) and the dynamic time warping approach (B). Difference between two curves plotted in red.

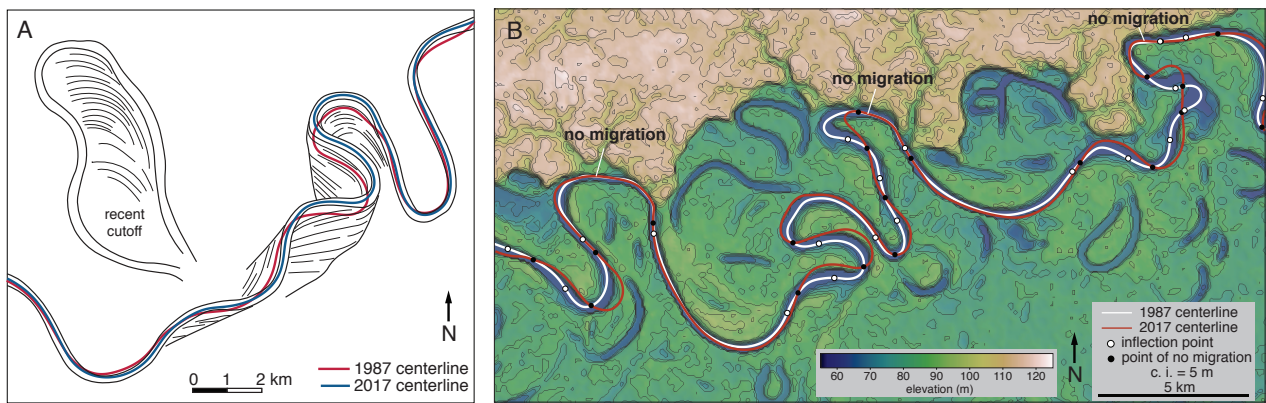


Figure 3: (A) Example of high migration rates that are probably associated with a recent cutoff, Juruá River. (B) Example of lower-than-expected migration rates where meanders run into the incisional boundaries of the channel belt, Purus River.

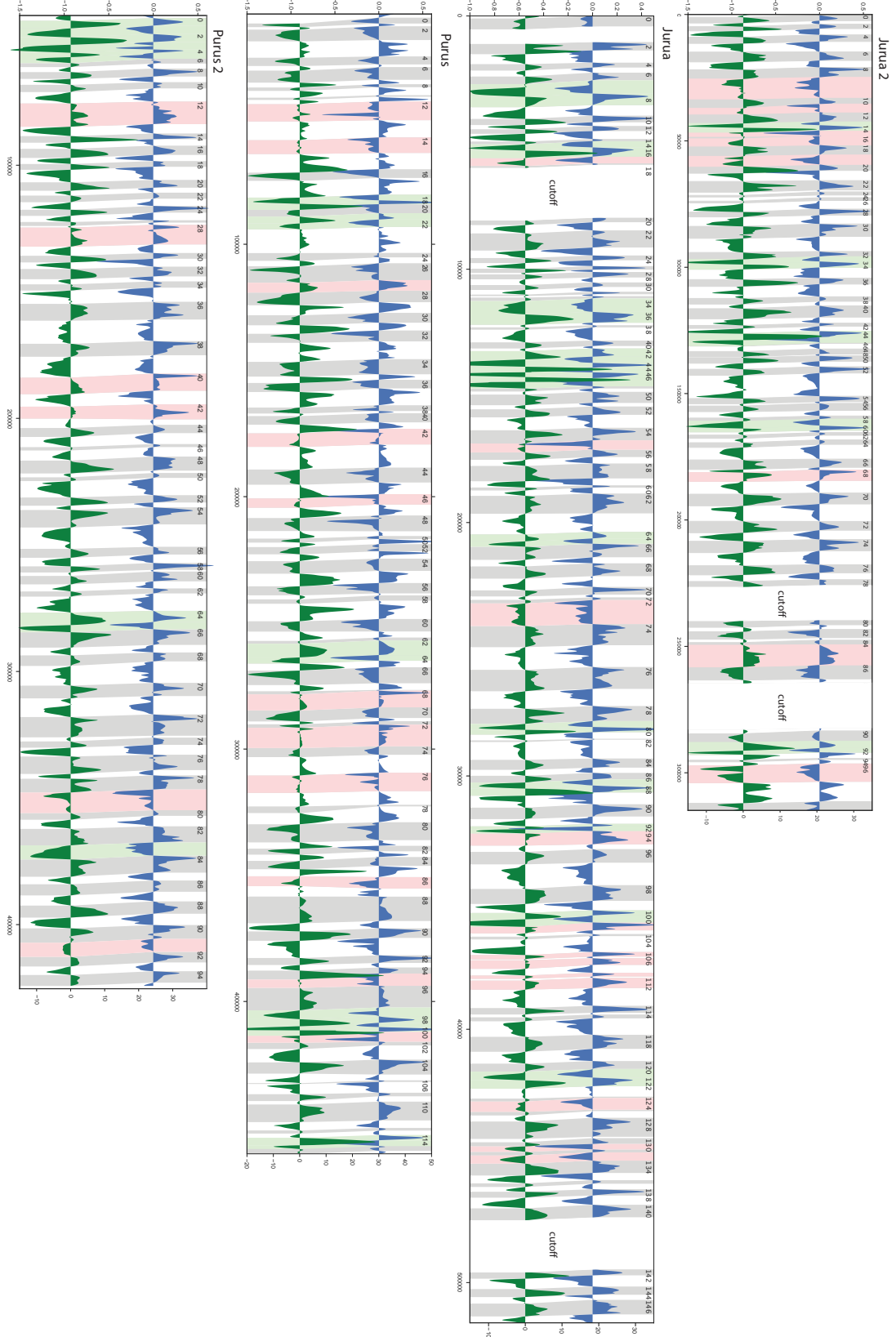


Figure 4: Variation of dimensionless curvature (blue) and actual migration rate (green) along the Juruá 2, Juruá, Purus, and Purus 2 channel segments. Migration rate scale shown on the right side, in m/years. Bends that are likely affected by recent cutoffs are highlighted in light green; bends that seem to be impacted by low erodibility are highlighted in red.

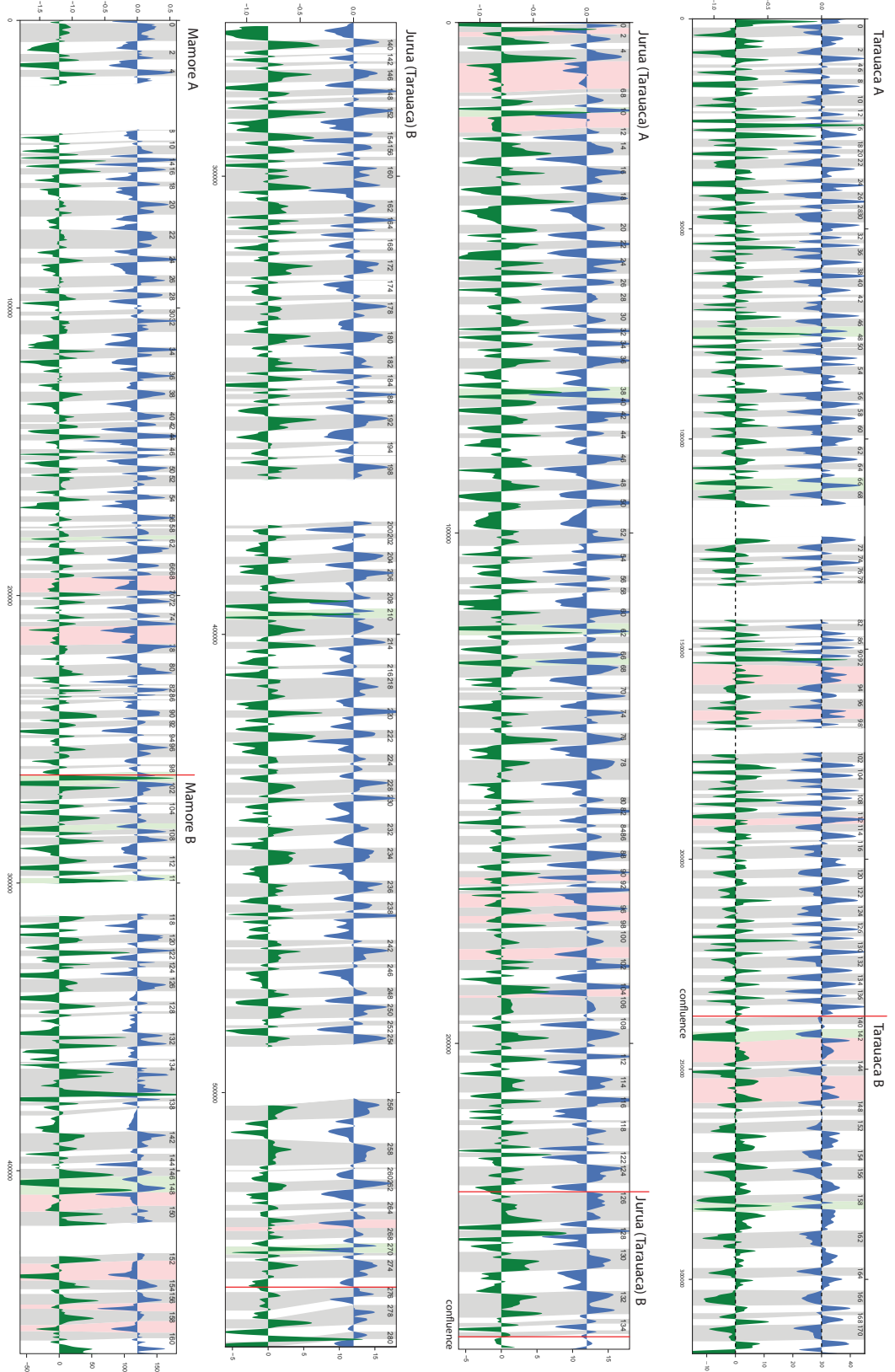


Figure 5: Variation of dimensionless curvature (blue) and actual migration rate (green) along the Tarauacá A, Tarauacá B, Juruá (Tarauacá) A, Juruá (Tarauacá) B, Mamoré A, and Mamoré B channel segments. Migration rate scale shown on the right side, in m/years. Bends that are likely affected by recent cutoffs are highlighted in light green; bends that seem to be impacted by low erodibility are highlighted in red.

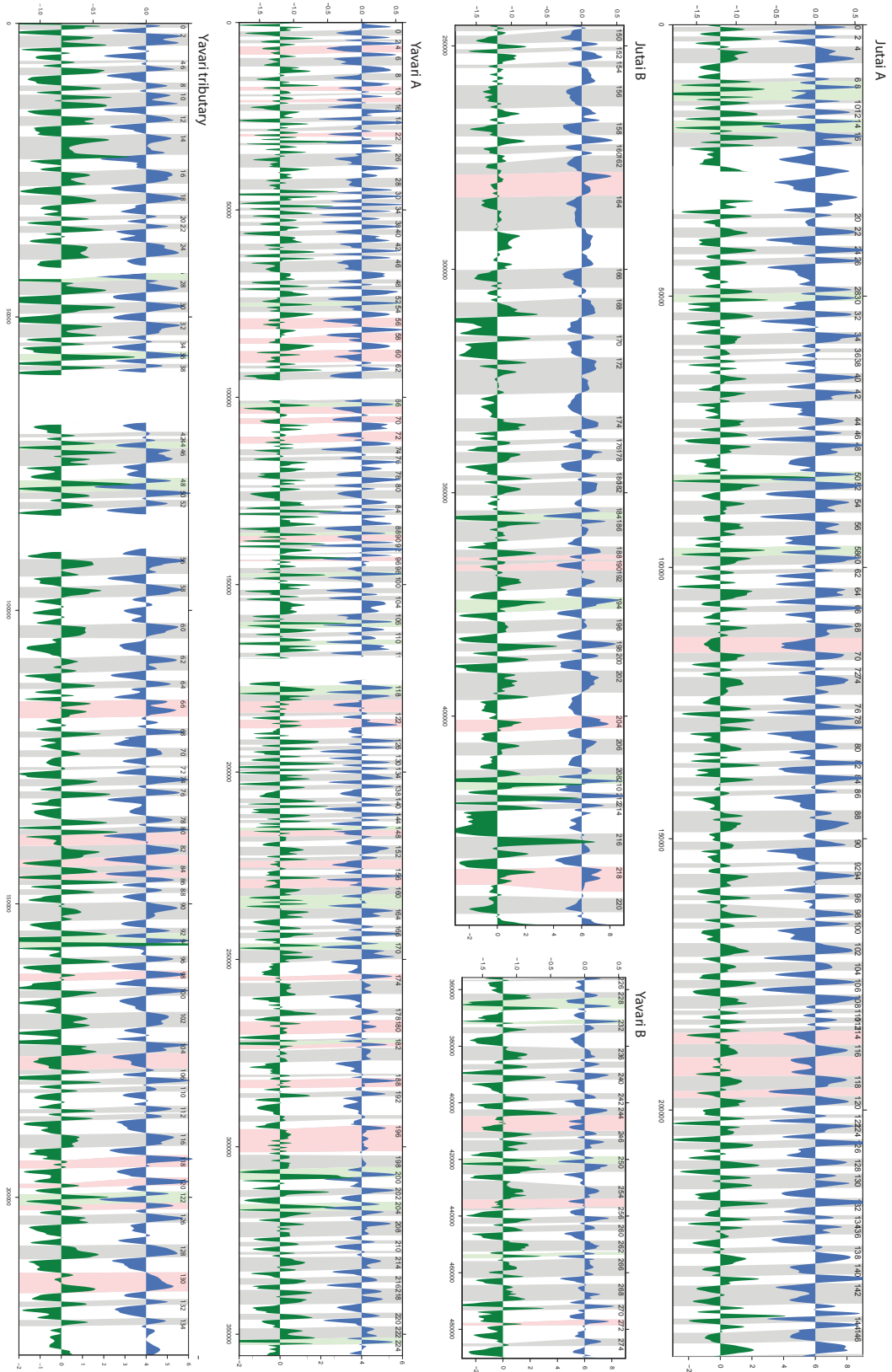


Figure 6: Variation of dimensionless curvature (blue) and actual migration rate (green) along the Jutaí A, Jutaí B, Yavarí B, Yavarí A, and Yavarí tributary channel segments. Migration rate scale shown on the right side, in m/years. Bends that are likely affected by recent cutoffs are highlighted in light green; bends that seem to be impacted by low erodibility are highlighted in red.

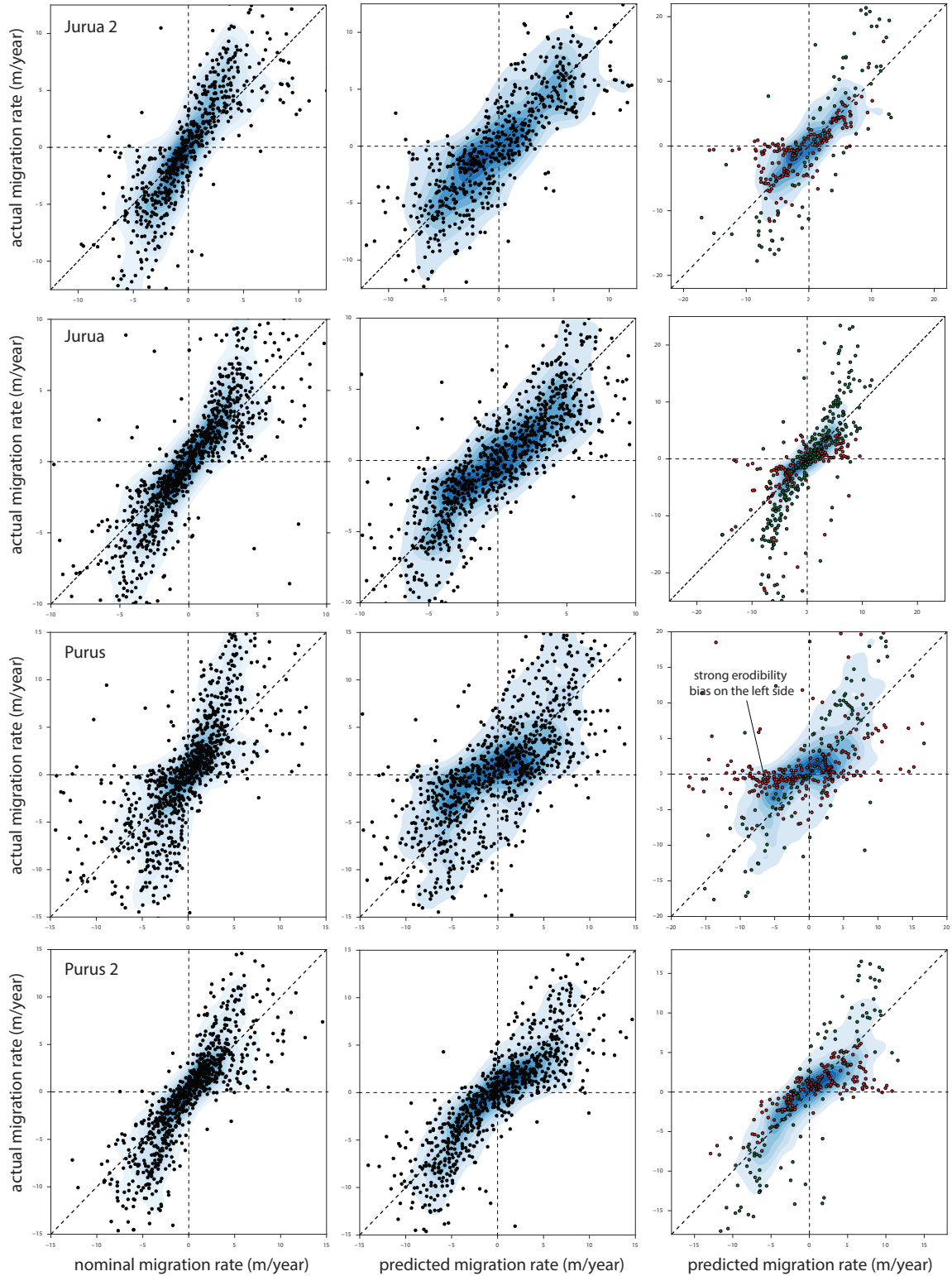


Figure 7: Plots of actual migration rate against nominal and predicted migration rates. Kernel density estimates are overlaid with scatterplots; only 5% of the data is shown in the scatter. In right-side panels, red dots highlight points affected by low erodibility and green dots highlight points related to recent cutoffs.

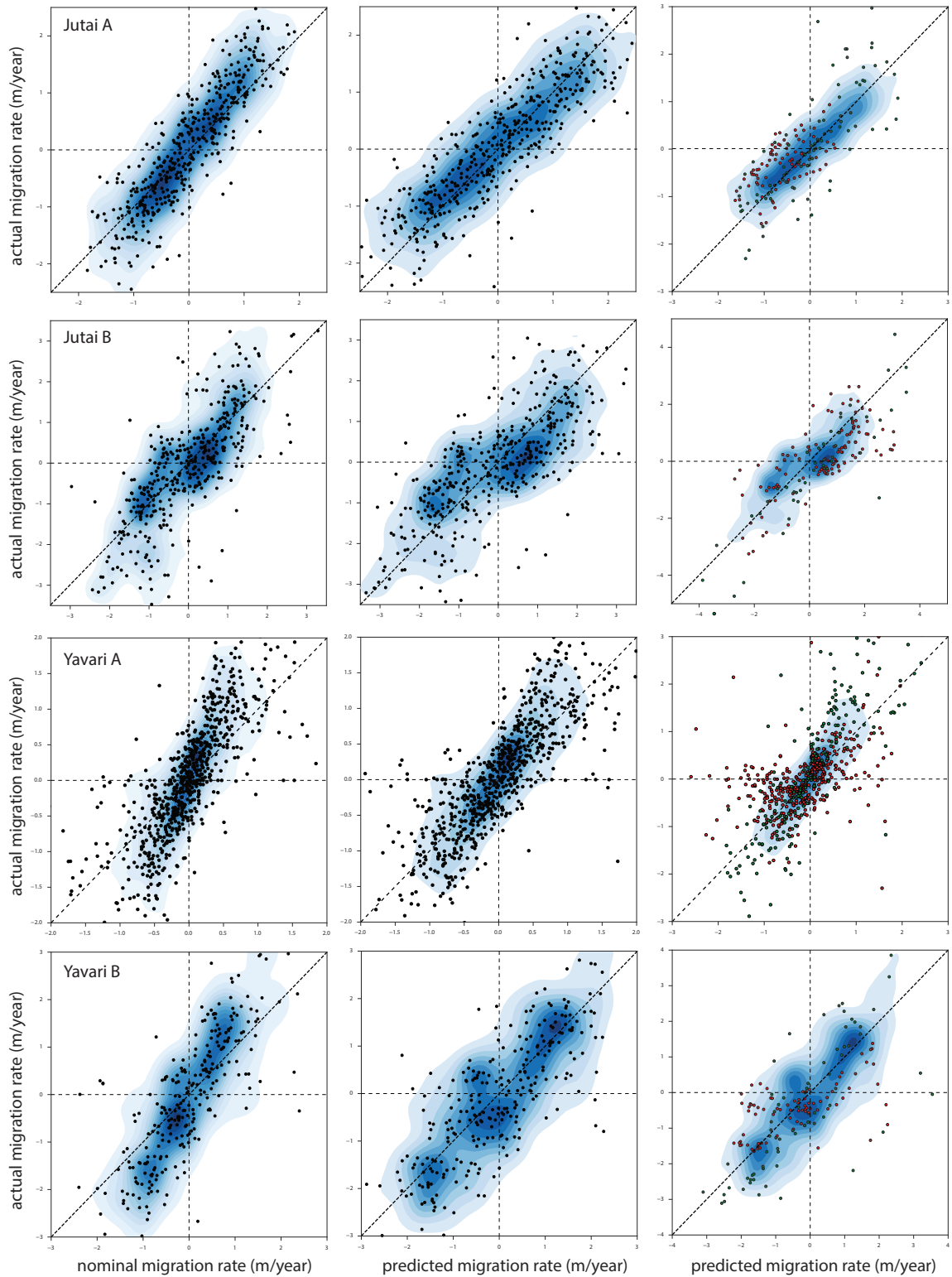


Figure 8: Plots of actual migration rate against nominal and predicted migration rates. Kernel density estimates are overlaid with scatterplots; only 5% of the data is shown in the scatter. In right-side panels, red dots highlight points affected by low erodibility and green dots highlight points related to recent cutoffs.

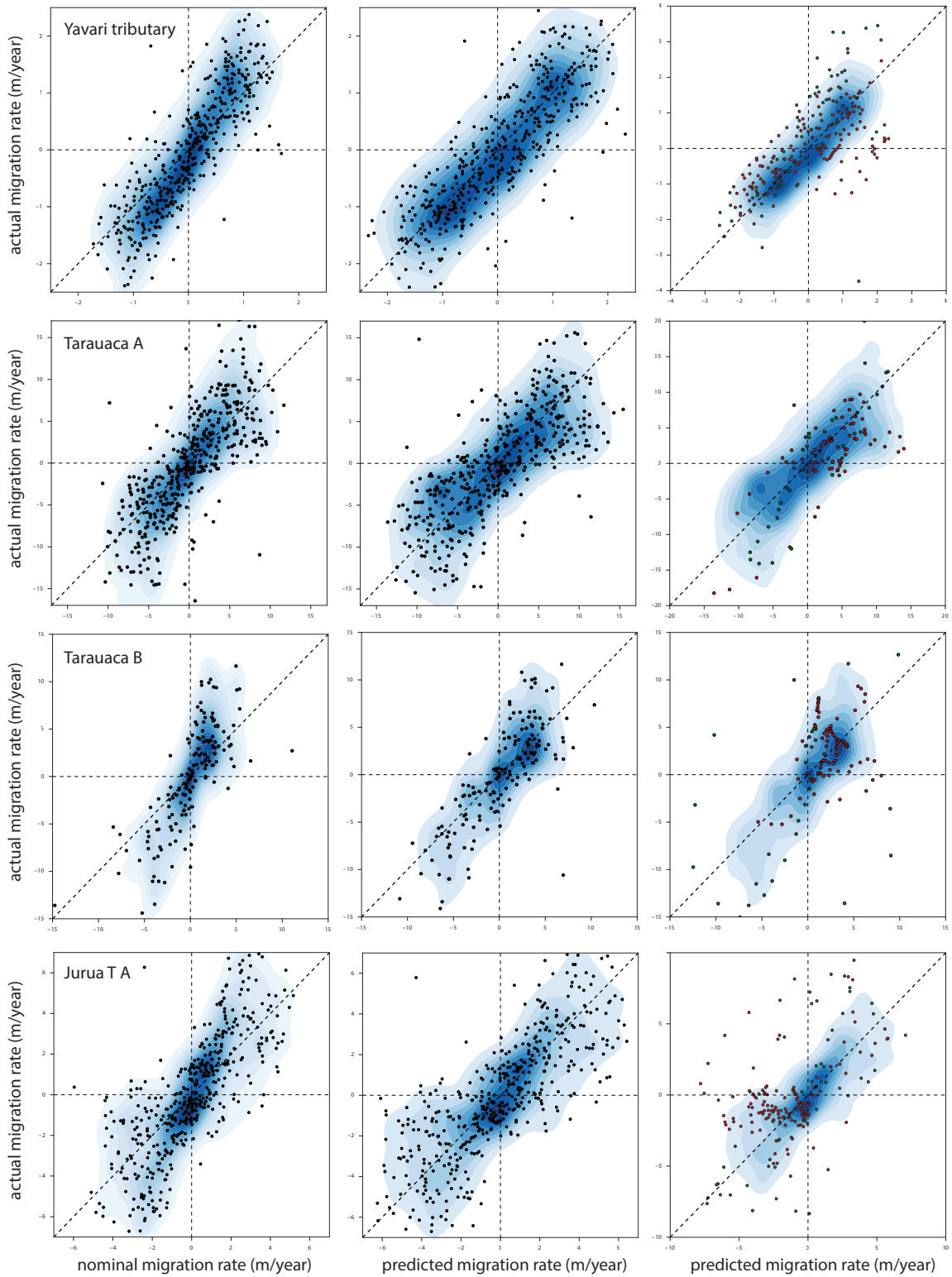


Figure 9: Plots of actual migration rate against nominal and predicted migration rates. Kernel density estimates are overlaid with scatterplots; only 5% of the data is shown in the scatter. In right-side panels, red dots highlight points affected by low erodibility and green dots highlight points related to recent cutoffs.

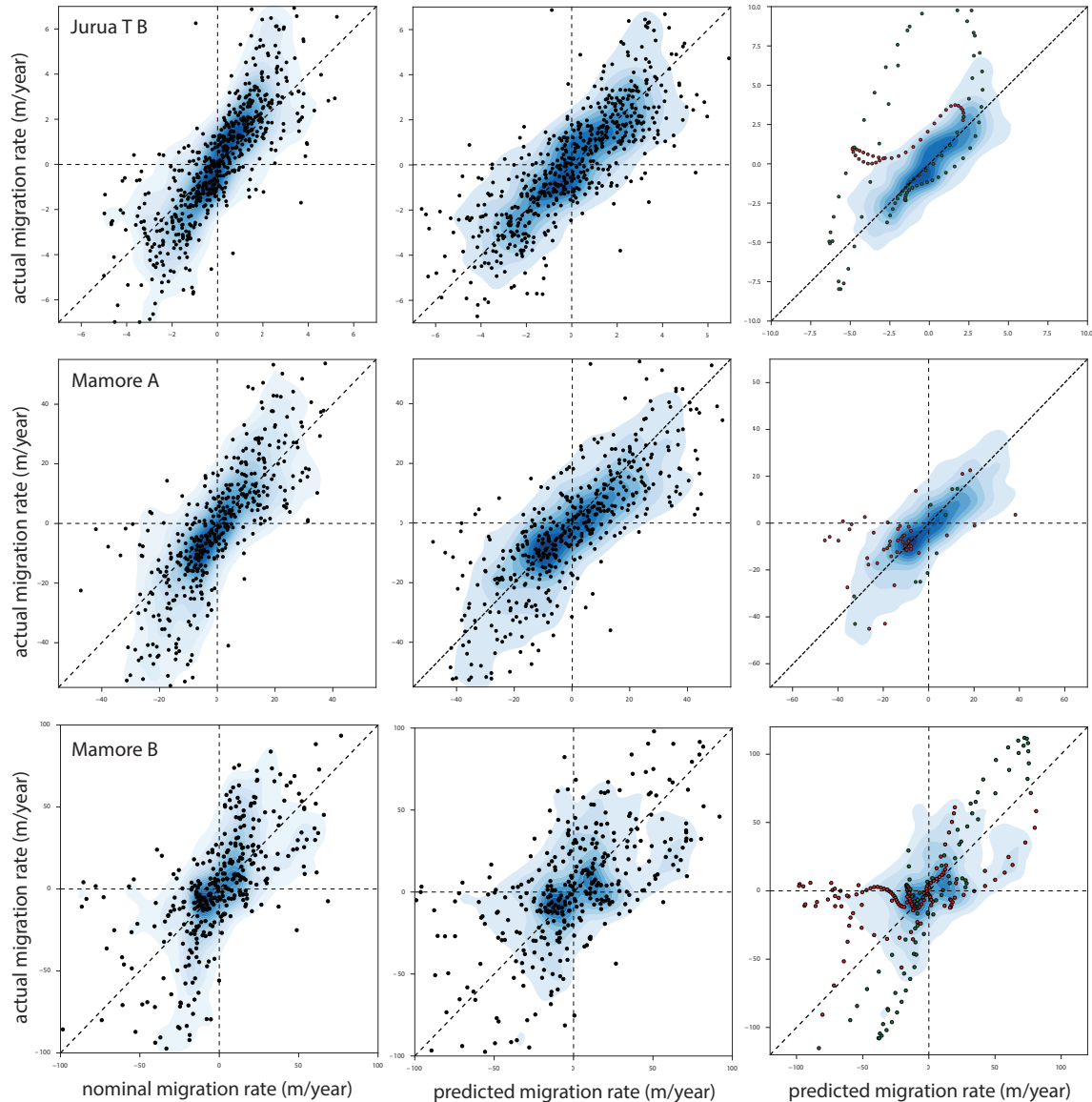


Figure 10: Plots of actual migration rate against nominal and predicted migration rates. Kernel density estimates are overlaid with scatterplots; only 5% of the data is shown in the scatter. In right-side panels, red dots highlight points affected by low erodibility and green dots highlight points related to recent cutoffs.

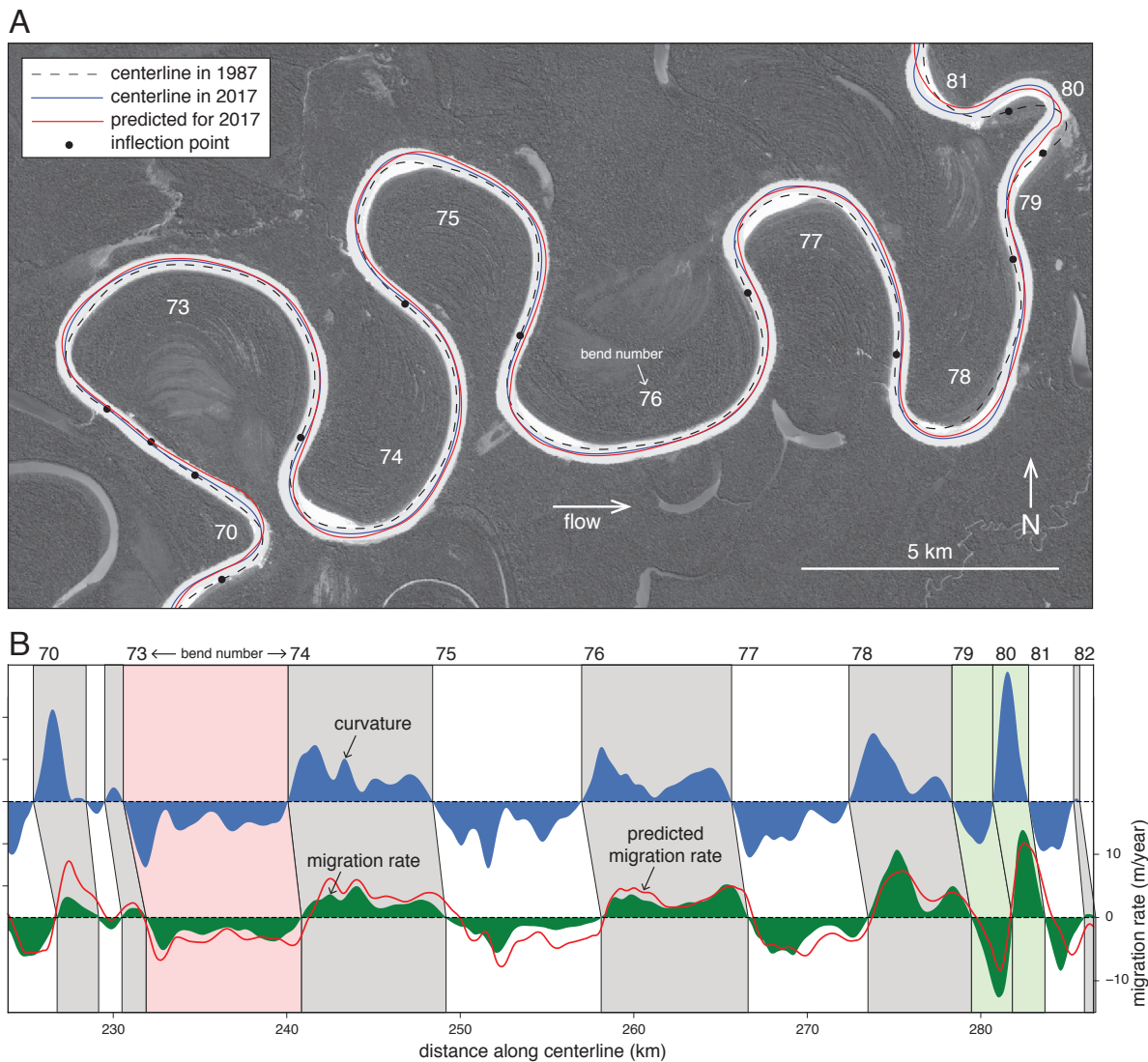


Figure 11: (a) Map-view comparison of predicted and actual channel locations for a segment of the Juruá River. (b) Curvature and migration rate for the same segment.

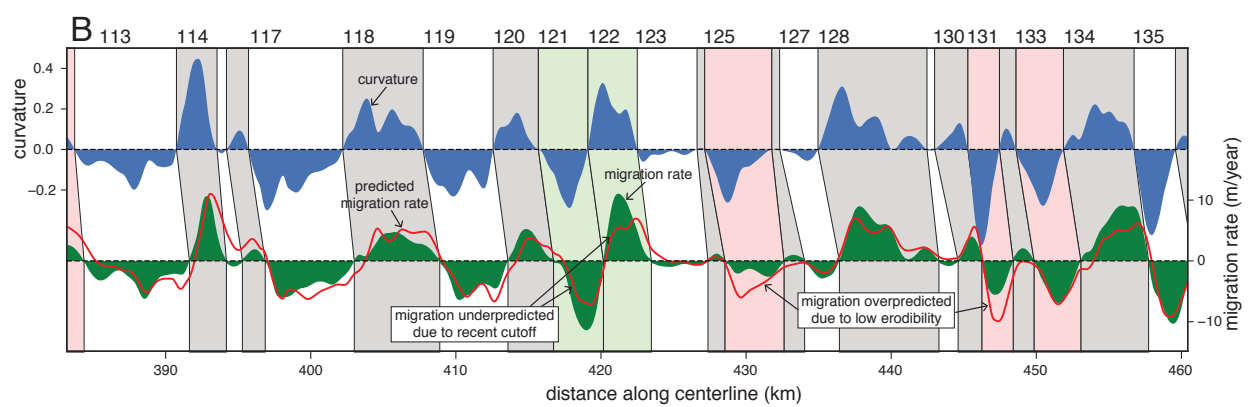
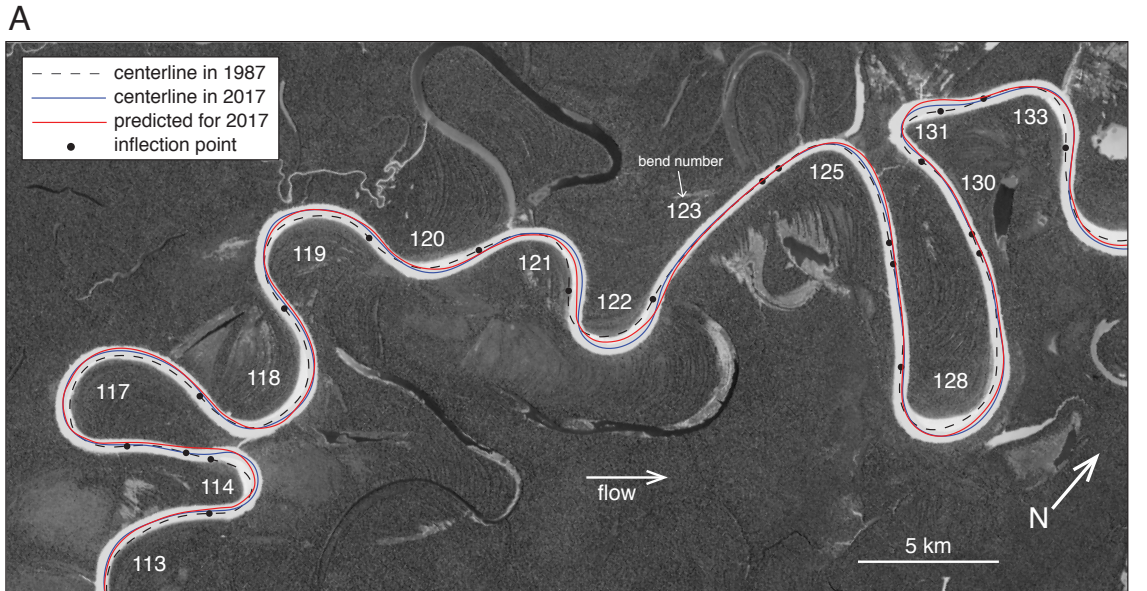


Figure 12: (a) Map-view comparison of predicted and actual channel locations for a second segment of the Juruá River. (b) Curvature and migration rate for the same segment.